Available online at www.sciencedirect.com
SCIENCE DIRECT®
Journal of Computational Physics 204 (2005) 692–714
JOURNAL OF COMPUTATIONAL PHYSICS
www.elsevier.com/locate/jcp

A compressible Navier–Stokes flow solver with scalar transport

Qibing Li [a,*], Song Fu [a], Kun Xu [b]

[a] Department of Engineering Mechanics, Tsinghua University, Beijing 100084, PR China
[b] Department of Mathematics, Hong Kong University of Science and Technology, Clear Water Bay, Kowloon, Hong Kong

Received 12 November 2003; received in revised form 11 October 2004; accepted 20 October 2004
Available online 23 November 2004

Abstract

This paper concerns the extension of the gas-kinetic scheme for the compressible Navier–Stokes equations to the flow calculation with interfaces and mixing. The objective of the current research targets mainly on the accurate capturing of Navier–Stokes diffusive interfaces, where the thickness can be resolved by the cell size. Firstly, a new BGK-NS scheme coupling with the level set type scalar function transport is constructed. Even though the scalar function is directly incorporated into the gas distribution function and it evolves according to the gas-kinetic equation, it likes more or less a color function, which has no direct contribution for the time evolution of conservative flow variables, such as mass, momentum and energy. Due to the coupling of the scalar function into the gas-kinetic formulation, the governing equations for the scalar function turns out to be an advection diffusion equations and the diffusive coefficient can be controlled by the particle collision time, which makes the current scheme suitable for the gas mixing problems with a controllable diffusion coefficients. However, for the non-mixing or sharp interface problems, such as the interface between gas and liquid, the current method can be used as a scheme similar to the level set method, where the interface location can be identified with a fixed level set value, such as $\Theta = 0$. The current method is applied to a few examples from the simple square wave propagation and diffusion to the 3D Rayleigh–Taylor instability. The supersonic mixing layer and the shock helium bubble interaction case show clearly the convergence of the current Navier–Stokes solver for the flow problems with mixing of components and interface once the interface thickness can be well resolved by the cell size. In the case of shock hitting SF6 cylinder, the computation predicts the experimental measure very well. In the current scheme, the Schmidt number can be freely chosen according to the physical reality.
© 2004 Elsevier Inc. All rights reserved.

MSC: 65M06; 76P05; 76N15
Keywords: Kinetic scheme; BGK equation; Chapman–Enskog expansion; Scalar convection–diffusion equation; Mixing layers

* Corresponding author. Tel.: +8610 62788674; fax: +8610 62772915.
E-mail address: lqb@tsinghua.edu.cn (Q. Li).

0021-9991/$ - see front matter © 2004 Elsevier Inc. All rights reserved.
doi:10.1016/j.jcp.2004.10.026

1. Introduction

Recently, based on the Bhatnagar–Gross–Krook (BGK) gas-kinetic model, an accurate Navier–Stokes flow solver has been developed in [1]. In the gas-kinetic scheme, the flux at the cell interface is calculated through the particle distribution function. This distribution function is a solution of the Boltzmann-BGK equation, where a non-equilibrium initial gas distribution function and an equilibrium state are constructed based on the cell averaged flow quantities. It has been shown that this method is equivalent to the Lax–Wendroff method for the Navier–Stokes equations in the well resolved smooth flow region. If the cell size is not fine enough to resolve the physical structure, the kinetic scheme provides automatically both *kinematic* and *dynamic* dissipation through the discontinuity at a cell interface and enlarged particle collision time according to the pressure jump at the cell boundary. Two desirable features of the kinetic approach are the positivity preserving property and the satisfaction of the entropy condition inherently, which guarantee the scheme to yield reliable numerical results in its application in the viscous flow computation, such as the hypersonic flow [2]. In order to calculate the chemical reactive flows, Lian and Xu [3] introduced a mass fraction variable in the gas-kinetic formulation as a new internal degree of freedom. This new variable can be used to describe fluid trajectory. But, due to the absence of non-equilibrium state in the initial gas distribution function, that scheme is accurate for the viscous flow under the condition of the computational time step being much larger than the particle collision time τ, i.e. $\Delta t \gg \tau$, which is invalid inside the shock layer. In order to increase the efficiency of the gas-kinetic BGK-NS method [1], Li and Fu [4] simplified the temporal evolution part of the gas distribution function, where a differentiation rather than an integration is used to evaluate the time evolution of the gas distribution function.

In the present paper, in order to capture accurately the flow evolution in the case of turbulent mixing and flow interfaces, a scalar variable is introduced in the gas-kinetic BGK model and the simplified kinetic scheme is used to solve this model equation. For the fluid-interface problem without mixing, the scalar function acts similarly as a level set function [5,6], which is most likely an interface indicator method. However, for the gas mixing problem due to the implementation of the scalar function in the kinetic governing equation, a convection–diffusion equation is equivalently solved for the scalar function, and the diffusion coefficient is controlled by the particle collision time. So, besides solving the compressible viscous governing equations, the objective of the current paper is to develop a scheme for the accurate capturing of the diffusive interface as well. The applicable regime for the current approach is the cases in which the fluid interfaces can be well resolved by the cell size. Otherwise, like many other TVD type shock capturing schemes, the numerical diffusion will take over the physical ones at the interfaces, and other numerical techniques have to be used to sharpen the interfaces.

2. Numerical method

2.1. BGK scheme with scalar transport

Even though the simulation results in this paper will include 3D cases, the following presentation of the kinetic scheme will be mainly in the 2D case. The 2D BGK-Boltzmann equation can be written as

$$f_t + uf_x + vf_y = \frac{g - f}{\tau}, \tag{1}$$

where f is the gas distribution function and g is the equilibrium state approached by f. They are both functions of space x, y, time t, particle velocities (u, v), and internal variable ξ. τ is the particle collision time. The equilibrium state is assumed to be a Maxwellian distribution,

$$g = \rho(\lambda/\pi)^{(K+3)/2}\,\mathrm{e}^{-\lambda((u-U)^2+(v-V)^2+(\theta-\Theta)^2+\xi^2)}, \tag{2}$$

where $\xi^2 = \xi_1^2 + \xi_2^2 + \cdots + \xi_K^2$ represents the internal energy of particles, and $\lambda = \rho/2p$. In this section, the capital letters are used to represent the macro quantities, such as the velocities U, V, and the lowercases for micro ones. The scalar variable Θ is implemented into the above formulation by assigning a new internal degree of freedom to the particle distribution function. Thus for a 2D flow, the total number of degrees of freedom K in ξ is equal to $(5-3\gamma)/(\gamma-1)+1$, which accounts for the independent rotational degrees of freedom and the random motion of particles in the z direction. Since mass, momentum and energy are conservative variables during particle collision, f and g satisfy the conservation constraint

$$\int (g-f)\psi\,\mathrm{d}\Xi = 0, \tag{3}$$

at any point in space and time. Here, $\mathrm{d}\Xi = \mathrm{d}u\,\mathrm{d}v\,\mathrm{d}\theta\,\mathrm{d}\xi$ is the volume element in the phase space with $\mathrm{d}\xi = \mathrm{d}\xi_1\mathrm{d}\xi_2\ldots\mathrm{d}\xi_K$, and ψ is the vector of moments

$$\psi = (\psi_1,\psi_2,\psi_3,\psi_4,\psi_5)^{\mathrm{T}} = (1,u,v,(u^2+v^2+\xi^2)/2,\theta)^{\mathrm{T}}. \tag{4}$$

Substituting Eq. (1) into Eq. (3) and taking the moments ψ, one can obtain the finite volume formulation

$$Q_{ij}^{n+1} = Q_{ij}^{n} + \frac{1}{\Delta x}\int_{t^n}^{t^n+\Delta t}(F_{i-1/2,j}-F_{i+1/2,j})\,\mathrm{d}t + \frac{1}{\Delta y}\int_{t^n}^{t^n+\Delta t}(G_{i,j-1/2}-G_{i,j+1/2})\,\mathrm{d}t, \tag{5}$$

where (i, j) are the cell index in the x and y directions, respectively. The relation between the distribution function f and the macroscopic conservative quantities Q and their fluxes F, G are given by

$$Q = (\rho,\rho U,\rho V,\rho\varepsilon,\rho\Theta)^{\mathrm{T}} = \int f\psi\,\mathrm{d}\Xi, \quad F = \int uf\psi\,\mathrm{d}\Xi, \quad G = \int vf\psi\,\mathrm{d}\Xi. \tag{6}$$

In the BGK scheme, the fluxes at the cell interface are calculated from the distribution function. If τ is a local constant, Eq. (1) has the integral solution

$$f(x,y,t,u,v,\theta,\xi) = \frac{1}{\tau}\int_0^t g(x',y',t',u,v,\theta,\xi)\,\mathrm{e}^{-(t-t')/\tau}\,\mathrm{d}t' + \mathrm{e}^{-t/\tau}f_0(x-ut,y-vt), \tag{7}$$

where $x' = x - u(t-t')$, $y' = y - v(t-t')$ is the trajectory of a particle motion and f_0 is the initial gas distribution function at the beginning of each time step ($t = 0$). If f_0 and g are obtained, one can easily calculate f from the above equation. Then the fluxes across the cell interface can be calculated through Eq. (6), where the flux for the scalar function is also included. To simplify the above method, a directional splitting method is adopted and the flux evaluation in the x direction is presented below. The coordinate of the interface between cell i and $i+1$ is assumed to be $x_{i+1/2} = 0$.

As presented in earlier approaches, f_0 and g around the cell interface can be constructed as

$$f_0(x) = g^l(1+a^l x - \tau(a^l u + A^l))(1-H[x]) + g^r(1+a^r x - \tau(a^r u + A^r))H[x] \tag{8}$$

and

$$g(x,t) = g_0(1 + (1-H[x])\overline{a}^l x + H[x]\overline{a}^r x + \overline{A}t), \tag{9}$$

where subscripts l, r denote the local quantity at the left and right sides of the cell interface, respectively. $H[x]$ is the Heaviside function. Here, g^l, g^r and g_0 are local Maxwellians. The terms a^l, a^r, $\overline{a}^l$, $\overline{a}^r$ and $\overline{A}$ are from the Taylor expansion of a Maxwellian and have the similar form, such as

$$a^l = a_1^l + a_2^l u + a_3^l v + a_4^l(u^2+v^2+\xi^2)/2 + a_5^l\theta, \tag{10}$$

where all coefficients $a_\alpha^l,\ldots,\overline{A}_\alpha$ ($\alpha = 1, 2, 3, 4, 5$) are local constants.

In order to evaluate the above coefficients, the conservative variables around each cell interface through the reconstruction from the cell averaged quantities have to be used,

$$\overline{Q}_i(x) = Q_i + L_s(Q_i - Q_{i-1}, Q_{i+1} - Q_i)(x - x_i). \tag{11}$$

Here, L_s is a slope limiter, such as the van Leer formulation. In the following, we are going to show the construction of the microscopic gas distribution function from the interpolated macroscopic variables. Firstly, with the above f_0 and g, a time-dependent gas distribution function f from Eq.(7) can be obtained,

$$\begin{aligned} f(0,t) = {} & C_1 g_0 + (t - C_1\tau)\overline{A} g_0 + (C_2 t - C_1\tau)\big(\overline{a}^l H[u] + \overline{a}^r(1 - H[u])\big) u g_0 \\ & + C_2((1 - u(t+\tau)a^r - \tau A^r)(1 - H[u])g^r) + C_2\big((1 - u(t+\tau)a^l - \tau A^l)H[u]g^l\big), \end{aligned} \tag{12}$$

where symbols C_1, C_2 are defined as $C_1 = 1 - \mathrm{e}^{-t/\tau}$, $C_2 = \mathrm{e}^{-t/\tau}$. The non-equilibrium terms in initial condition f_0, such as $-\tau(a^l u + A^l)g^l$ and $-\tau(a^r u + A^r)g^r$, account for the deviation of a gas distribution function away from a Maxwellian, and have no direct contribution to the conservative variables,

$$\int (a^l u + A^l)\psi g^l \,\mathrm{d}\Xi = 0, \quad \int (a^r u + A^r)\psi g^r \,\mathrm{d}\Xi = 0. \tag{13}$$

The coefficient a^l_β ($\beta = 1, 2, 3, 4, 5$) can be calculated by

$$\frac{\overline{Q}_i(0) - \overline{Q}_i(-\Delta x^l)}{\rho^l \Delta x^l} = \frac{1}{\rho^l}\int \psi a^l g^l \,\mathrm{d}\Xi = M^l_{\alpha\beta} a^l_\beta, \tag{14}$$

where $\Delta x^l = x_{i+1/2} - x_i$ and $M^l_{\alpha\beta} = (1/\rho^l)\int \psi_\alpha \psi_\beta g^l \,\mathrm{d}\Xi$. The details to solve Eq. (14) can be found in Appendix A. Then from (13), A^l_β, A^r_β can be calculated similarly as

$$M^l_{\alpha\beta} A^l_\beta = -\frac{1}{\rho^l}\int a^l u \psi_\alpha g^l \,\mathrm{d}\Xi. \tag{15}$$

At ($x = 0$, $t = 0$), the compatibility condition Eq. (3) gives

$$Q_0 = \int g_0 \psi \,\mathrm{d}\Xi = \int_{u>0} g^l \psi \,\mathrm{d}\Xi + \int_{u<0} g^r \psi \,\mathrm{d}\Xi - \int_{u>0} \tau(a^l u + A^l) g^l \psi \,\mathrm{d}\Xi - \int_{u<0} \tau(a^r u + A^r) g^r \psi \,\mathrm{d}\Xi. \tag{16}$$

Note that the last two terms in the above equation are ignored in the scheme of [1]. After having Q_0, the coefficient $\overline{a}^l_\beta$ can be obtained by

$$\frac{Q_0 - \overline{Q}_i(-\Delta x^l)}{\rho_0 \Delta x^l} = M^0_{\alpha\beta}\overline{a}^l_\beta, \tag{17}$$

where $M^0_{\alpha\beta} = (1/\rho_0)\int \psi_\alpha \psi_\beta g_0 \,\mathrm{d}\Xi$. The coefficients a^r_β and $\overline{a}^r_\beta$ can be calculated similarly.

To determine $\overline{A}$, Xu [1] used the integration of the conservation constraint (3) at ($x = 0$) over the whole time step, which leads to an equation with eleven terms at the right-hand side. In the current approach, a simple method in [4] is used through the differentiation of (3) at ($x = 0$, $t = 0$),

$$\frac{\partial}{\partial t}\int [g(0,t) - f(0,t)]\psi_\alpha \,\mathrm{d}\Xi|_{t=0} = 0. \tag{18}$$

Substituting (9) and (12) into the above equation, and using (16), a simplified equation for $\overline{A}$ is obtained,

$$M^0_{\alpha\beta}\overline{A}_\beta = -\frac{1}{\rho_0}\int \left[a^l H[u] u g^l + a^r(1 - H[u]) u g^r\right]\psi_\alpha \,\mathrm{d}\Xi. \tag{19}$$

The evaluation of $\bar{A}$ is incidently similar to previous method [7,8], where a different consideration is imposed. However, in the current method, the effect of non-equilibrium state is taken into account, which is necessary to capture the viscous solution.

The collision time τ in the current method is given by

$$\tau = \mu_0/p_0 + C_1\Delta t(p^l - p^r)/(p^l + p^r), \tag{20}$$

where μ_0 and p_0 are the macroscopic viscosity coefficient and the pressures calculated from Q_0. The last term in the above equation represents the artificial dissipation and the constant C_1 can be chosen from 0 to 1 to control the dynamic dissipation. The time step Δt is calculated from the CFL condition. It is shown (see Appendix B) that to the Navier–Stokes order, the diffusion coefficient for the scalar function equals to the viscosity coefficient $D = \nu$, or the Schmidt number $Sc = \nu/D$ becomes unity. However, with the introduction of a collision time τ_s in the next subsection, the Schmidt number in the current scheme can be adjusted to any value.

Finally, the numerical fluxes can be calculated in Eq. (6), where f is given by Eq. (12). The conservative variables at the next time step are updated through the finite volume formulation (5).

2.2. Scalar transport computation with a variable Schmidt number

Theoretically, the gas-kinetic scheme presented in the last section can be faithfully used to update the conservative variables, as well as the scalar function by taking the moments $u\psi$ to the gas distribution function at a cell interface. Practically, since the passive scalar or the level set function will not effect the conservative flow evolution, the flux function in the last subsection can be re-organized and the original scheme BGK-NS method without scalar function can be used directly. Furthermore, the re-arranged formulation has the freedom to modify the diffusion coefficient for the scalar function and the Schmidt number.

The main difference between the BGK scheme presented in the last section and the one without including the scalar transport comes from the terms related to spatial and temporal gradients of the scalar function. Firstly, the spatial slope term (see Appendix A) can be rewritten as

$$a_1 = a_1' - \Theta a_5, \quad a_1' = b_1 - Ua_2 - Va_3 - C_1 a_4. \tag{21}$$

Here, a_1' is the one used in the BGK-NS method [1], where the scalar transport is not included. The changing of the coefficients from (a_1, a_2, a_3, a_4) to (a_1', a_2, a_3, a_4), similarly for A, will not alter the corresponding flux functions for the mass, momentum, and energy in the last subsection, which are identical to the fluxes of the BGK-NS method. These fluxes are denoted by $F_\rho', F_{\rho U}', F_{\rho V}', F_{\rho E}'$. Now let's rewrite the flux function F_Θ of passive scalar Θ. Based on the formulation in the last section, the terms related to the spatial and temporal slopes in F_Θ is

$$\begin{aligned} T_{au5} &= \int au\psi_5 g\,\mathrm{d}\Xi = \int (a_1 + a_2u + a_3v + a_4(u^2+v^2+\xi^2)/2 + a_5\theta)u\theta g\,\mathrm{d}\Xi \\ &= \int (a_1' + a_2u + a_3v + a_4(u^2+v^2+\xi^2)/2)u\theta g\,\mathrm{d}\Xi + \int a_5(\theta^2 - \Theta\theta)ug\,\mathrm{d}\Xi \\ &= \langle\theta\rangle T_{au1}' + a_5\rho\langle u\rangle(\langle\theta^2\rangle - \Theta\langle\theta\rangle) = \Theta T_{au1}' + a_5 p\langle u\rangle, \end{aligned} \tag{22}$$

where $\rho\langle\ldots\rangle = \int(\ldots)g\mathrm{d}u\mathrm{d}v\mathrm{d}\xi$ and the detailed formulation can be found in the appendix of [1]. The symbol T'_{au1} is the corresponding term in the BGK-NS scheme without including scalar function, which is

$$T_{au1}' = \int (a_1' + a_2u + a_3v + a_4(u^2+v^2+\xi^2)/2)u\psi_1 g\,\mathrm{d}\Xi. \tag{23}$$

Actually, one can see that

$$T_{au1}' = \int au\psi_1 g\,\mathrm{d}\Xi = T_{au1}, \tag{24}$$

which reveals the fact that the passive scalar function will not affect the fluxes of other flow variables. Similarly,

$$T_{au^25} = \int au^2\psi_5 g\,\mathrm{d}\Xi = \langle\theta\rangle T'_{au^21} + a_5 p\langle u^2\rangle, \tag{25}$$

$$T_{a5} = \int a\psi_5 g\,\mathrm{d}\Xi = \langle\theta\rangle T'_{a1} + a_5 p, \tag{26}$$

$$T_{A5} = \int A\psi_5 g\,\mathrm{d}\Xi = \langle\theta\rangle T'_{A1} + A_5 p. \tag{27}$$

Therefore, we can express the flux for the scalar function as

$$\begin{aligned} F_\Theta = {} & C_1\rho_0 U_0\Theta_0 + (t - C_1\tau_s)(\Theta_0 T'_{\overline{A}u1} + \overline{A}_5 U_0 p_0) + (C_2 t - C_1\tau_s)[\Theta_0(T'_{\overline{a}^l u^2 1} + T'_{\overline{a}^r u^2 1}) \\ & + p_0(\overline{a}_5^l\langle u^2\rangle^0_{u>0} + \overline{a}_5^r\langle u^2\rangle^0_{u<0})] + C_2(\rho^l\Theta^l\langle u\rangle^l_{u>0} + \rho^r\Theta^r\langle u\rangle^r_{u<0}) - C_2(t+\tau_s)(\Theta^l T'_{a^l u^2 1} + \Theta^r T'_{a^r u^2 1} \\ & + p^l a_5^l\langle u^2\rangle^l_{u>0} + p^r a_5^r\langle u^2\rangle^r_{u<0}) - C_2\tau_s(\Theta^l T'_{A^l u1} + \Theta^r T'_{A^r u1} + p^l A_5^l\langle u\rangle^l_{u>0} + p^r A_5^r\langle u\rangle^r_{u<0}), \end{aligned} \tag{28}$$

where $\langle\cdots\rangle^l_{u>0}$, $\langle\cdots\rangle^r_{u>0}$, and $\langle\cdots\rangle^0$ denote the moments taken on g^l, g^r, and g_0.

In summary, in the original BGK-NS scheme without scalar transport, we have already obtained all terms related to T'. The corresponding flux for the scalar can be simply assembled by the above formula. Note the above flux for $\Theta$is equivalent to that from the fully coupled scheme in the last subsection.

In a well resolved flow region, all quantities have a smooth distribution across a cell interface. In such a case, $g^l = g^r = g_0$, $a^l = a^r = \overline{a}^l = \overline{a}^r$, and $A^l = A^r = \overline{A}$ hold, and the gas distribution function at a cell interface becomes

$$f = g_0[1 - \tau(\overline{a}u + \overline{A}) + \overline{A}t]. \tag{29}$$

In this situation, the flux for the scalar function goes to

$$F_\Theta = \Theta_0 F'_\rho - \overline{a}_5\tau_s p_0\langle u^2\rangle^0 + \overline{A}_5(t - \tau_s)p_0 U_0, \tag{30}$$

where τ_s can be chosen according to the diffusion coefficient $D = \tau_s p/\rho$. Therefore, the code for the equations with scalar transport can be easily constructed from the original one without scalar function, and the only additional term is the above flux evaluation for Θ. The other fluxes, such as mass, momentum and energy, are the same as those in the BGK-NS scheme. More importantly, through this separation, the collision time for the scalar function can be calculated separately according to the diffusion coefficient D. Thus, the present scheme can simulate the flow with different Schmidt numbers. In this scheme, the non-equilibrium state is included in the initial condition at the beginning of each computational time step. Therefore, the current method is truly a NS flow solver in both cases of $\Delta t > \tau$ and $\Delta t < \tau$, and the influence of time step Δt on the accuracy of the viscous solution is reduced to a minimal level.

The present scheme can be shown to have second-order accuracy for the Navier–Stokes solutions [9]. The boundary condition can be directly implemented in the current method, such as the slip, non-slip, isothermal, and adiabatic. For example, the slip boundary condition is successfully used in the micro-channel flow computation [10]. As the BGK model corresponds to unit Prandtl number, the BGK scheme can have any realistic value with the modifications of heat flux in the total energy transport. The details of Prandtl number fix for the BGK scheme can be found in [1].

3. Numerical experiments

In order to verify the gas-kinetic scheme with the scalar transport, several cases have been tested in this section. The main application of the current method is for the interface mixing problem, where the

physically diffused interface can be resolved by the cell size. But, in the last three cases, the scalar function is also used, similar to a level set function, to identify the flow interfaces.

3.1. Blast wave

The Woodward–Colella blast wave interaction is tested first [11], with the scalar function is used to indicate the location of initial gas separation. The computational domain is $0 \leqslant x \leqslant 800$ and the flow-field is initialized by stationary air with equal density $\rho = 1$ and different constant pressure in different regions between reflecting walls: 1000 in the left, 100 in the right, and 0.01 in the mid region $80 \leqslant x \leqslant 720$. The scalar function has a value of unity in the middle region and zero otherwise. Fig. 1 shows the flow field at time $t = 30$, where the complicated wave structures have been captured. The scalar function shows the locations of two contact discontinuity wave and the gas separation.

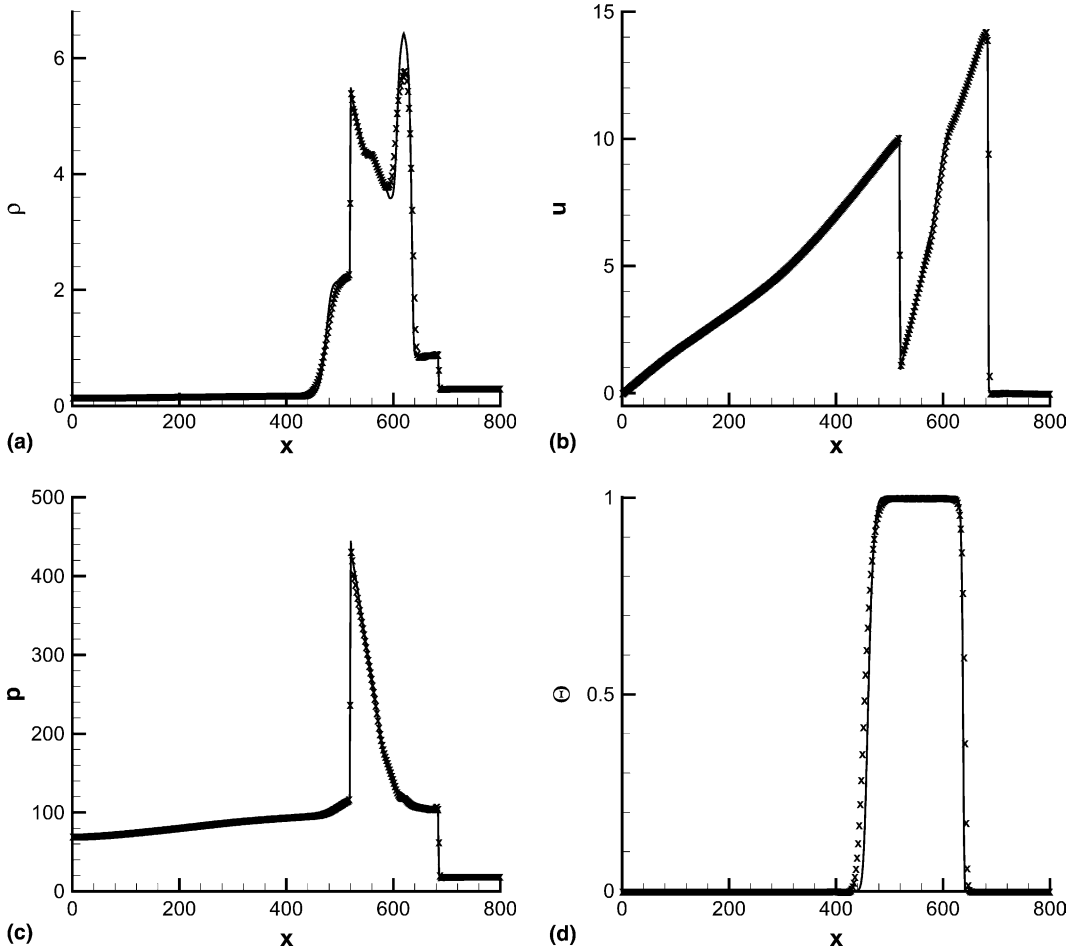

Fig. 1. Woodward–Colella case solutions at time $t = 30$: (a) density, (b) velocity, (c) pressure, and (d) scalar function. The solutions marked with symbols are obtained from 400 mesh points and solid lines are from 800 points.

3.2. Square wave convection and diffusion

Consider the scalar transport equation

$$\Theta_t + U\Theta_x + V\Theta_y = D(\Theta_{xx} + \Theta_{yy}) \tag{31}$$

with initial condition

$$\Theta = \begin{cases} 1 & \text{if } \alpha \leqslant x \leqslant \beta \text{ and } \alpha \leqslant y \leqslant \beta, \\ 0 & \text{else,} \end{cases} \tag{32}$$

where α, β are constants, the analytical solution can be found as

$$\Theta(x,y,t) = \frac{1}{4}\left\{\operatorname{erf}\left(\frac{\beta - x'}{2\sqrt{Dt}}\right) + \operatorname{erf}\left(\frac{-\alpha + x'}{2\sqrt{Dt}}\right)\right\}\left\{\operatorname{erf}\left(\frac{\beta - y'}{2\sqrt{Dt}}\right) + \operatorname{erf}\left(\frac{-\alpha + y'}{2\sqrt{Dt}}\right)\right\} \tag{33}$$

with $x' = x - Ut$, $y' = y - Vt$. This gives the convection and diffusion of an initial square wave. In the present study, the computational domain is chosen as $[0,1]\times[0,1]$ with parameters $U = V = 100$, $\alpha = 0.175$, and $\beta = 0.225$. The boundary values are implemented according to the above theoretical solution. The cell size is uniform with $\Delta x = \Delta y = 0.0125$. Fig. 2 shows the comparison of the present numerical results for diffusion coefficient $D = 2$ and $D = 1.5$ with the exact solutions. Both computational and exact solutions are almost identical to each other, which shows the good accuracy of the present scheme in the simulation of scalar convection and diffusion. It also demonstrates the validity of the Schmidt number control in the present scheme. The mesh refinement solution are shown in Fig. 3.

To further verify the accuracy of the present scheme, the error norms are calculated with different cell size $\Delta x(=\Delta y)$. The computations are all started from the analytical solution at time $t = 2\times10^{-3}$, and the time step sizes are fixed to a small value, $\Delta t = 1.4\times10^{-6}$. Here, the limiter in the reconstruction procedure is not adopted and the variables at the cell interface are obtained by the simple linear interpolation method. The error norms L_2 and L_∞ at $t = 4\times10^{-3}$ are presented in Fig. 4(a), which show that the present scheme has second-order accuracy in space. Similarly the error norms with different computational time step size are calculated with a fine mesh $\Delta x = 1/1280$. For simplicity the error norms are computed after only one

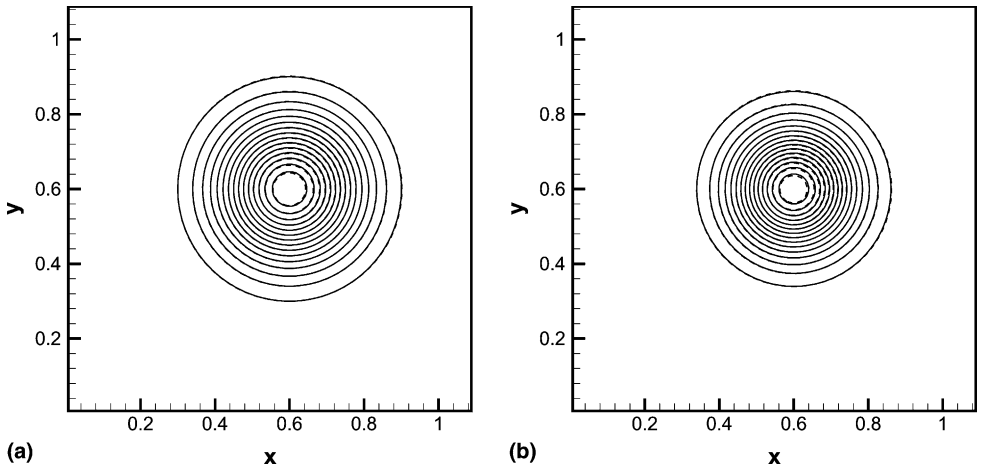

Fig. 2. Distribution of scalar function at time $t = 4\times10^{-3}$. Figure (a) is for diffusion coefficient $D = 2$ and (b) for $D = 1.5$. The dashed lines are from the present calculation and the solid lines represent the exact solution.

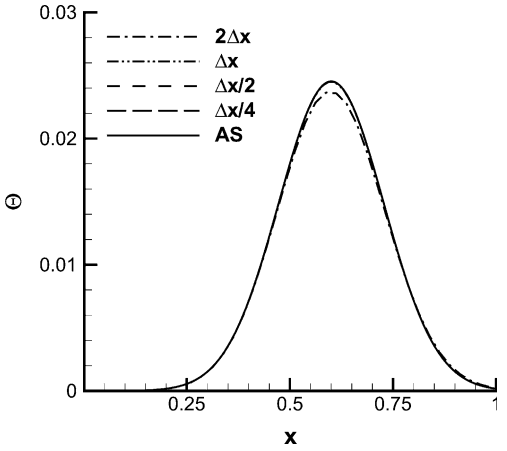

Fig. 3. Scalar distribution along $y = 0.6$ at time $t = 4 \times 10^{-3}$. Symbol 'Δx' represents results from the cell size $\Delta x = \Delta y = 0.0125$, '$2\Delta x$' for the size $\Delta x = \Delta y = 0.025$, and so on. 'AS' is the analytical solution.

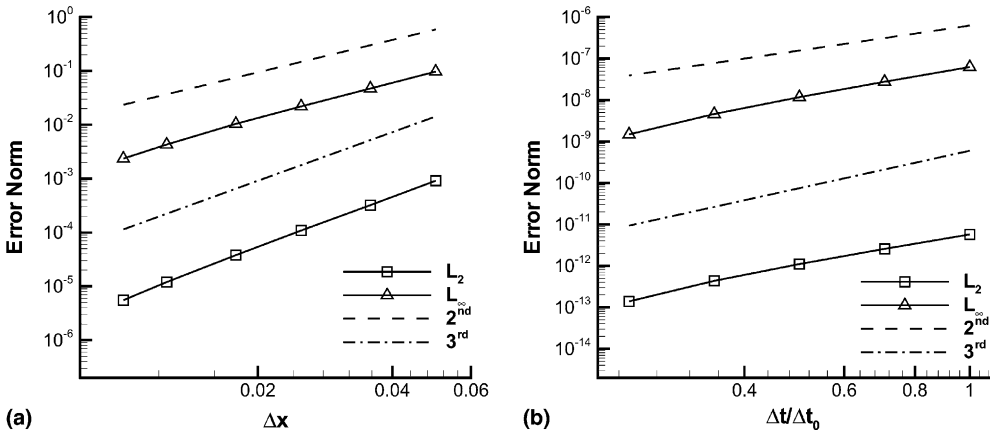

Fig. 4. Variations of error norms with: (a) computational cell size; (b) time step. The lines symbolized by '2^{nd}' and '3^{rd}' indicate the trends of the second-order and third-order accurate schemes, respectively. Both the L_2 and L_∞ norms are normalized by the instantaneous maximal value. The values calculated with $\Delta x = 1/320$ are subtracted from the error norms in (a). Δt_0 in (b) is computed with Courant number equal to unity.

time step started from $t = 2 \times 10^{-3}$. The results in Fig. 4(b) show that the present scheme is more than second-order accurate in time, which is consistent with the study of Ohwada [9].

3.3. High-speed mixing layer

Turbulent mixing layers are commonly observed in various engineering applications such as combustion, propulsion and environmental flows. The rich flow physics thus attracted numerous experimental [12–14] and computational studies [15,16]. These results show that with increasing convective Mach number M_c, the normalized growth rate, which is defined as the free-stream velocity difference to the sum of the sound speeds, decreases rapidly. Although the flow is 3D, 2D simulation with BGK scheme can still capture the

growth rate decrease. Large-scale structures have been found in 2D high M_c mixing layer simulations [17–19].

In the present study, the BGK scheme with scalar transport is applied in the spatially developing high-speed mixing layer calculation, where the scalar is introduced to study the mixing of the fluids. The computational conditions are similar to case 3 of [18] ($M_c = 0.4$) except that the Prandtl number equals to 0.7 and the Schmidt number is $Sc = 1$. The value for the scalar is set to unity in the high-speed side flow region and zero in the other side. The cell size is uniform in the horizontal direction $\Delta x = 0.296$ and stretched in the vertical direction with $\Delta y_{\min} = 0.2$ near the centerline $y = 0$. Fig. 5 shows the instantaneous flow-field in which one can easily identify the large flow structures. In general, the flow loses its stability at the upstream, then vortices form, roll up, and interact with each other while the flow moves to the downstream. The mixing layer grows through the pairing of neighboring vortices. With the present broadband forcing imposed at the inflow, the mixing layer grows almost linearly (see Fig. 6) and the center of the mixing layer moves to the low-speed side gradually. The normalized growth rate based on the momentum thickness $(d\delta_m/dx)(U_1 + U_2)/(U_1 - U_2)$ in the fully developed region is about 0.028, the corresponding vorticity thickness growth rate is about 0.12, which agree well with the experimental value of Goebel and Dutton [20]. This growth rate also shows a little decrease when compared with that of mixing layer with Prandtl number $Pr = 1.0$ [18]. The results below calculated with a coarse mesh ($\Delta x = 0.592$, $\Delta y_{\min} = 0.4$), i.e., the mean flow-field, the fluctuation of the velocity, and the scalar function, show good mesh convergence.

It is known that a fully developed turbulent mixing layer evolves to self-similarity with a linear growth thickness. The statistics of flow qualities are obtained here with time averaging of about six maximal time scales $T = L_x/U_c$, where $U_c = (U_1 + U_2)/2$ is the convective velocity of the free streams. Fig. 7(a) shows the self-similar mean velocity distributions calculated at different far-field streamwise locations. The collapse of the data onto a single curve is excellent and this curve is almost identical to the error function profile, which is the first-order approximation to the velocity in incompressible mixing layer. The mean scalar function concentration profiles shown in Fig. 7(b) also exhibit good similarity but with a different character when compared with the velocity profiles: they have three inflection points while only one for the mean velocity. This observation is consistent with the experimental results [21,22] and other numerical results [23,24]. The triple inflection points are correlated with the non-marching PDF of the scalar fluctuations [22], which

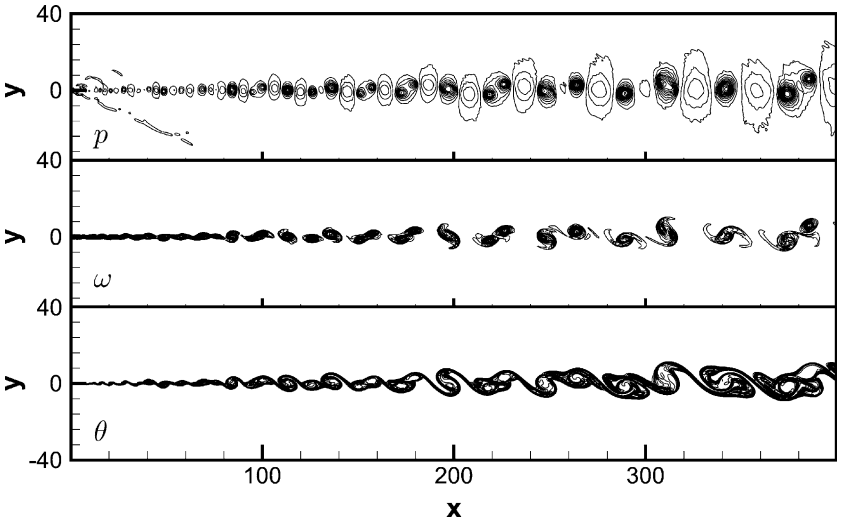

Fig. 5. Instantaneous pressure, vorticity and passive scalar concentration contours in mixing layers with $M_c = 0.4$.

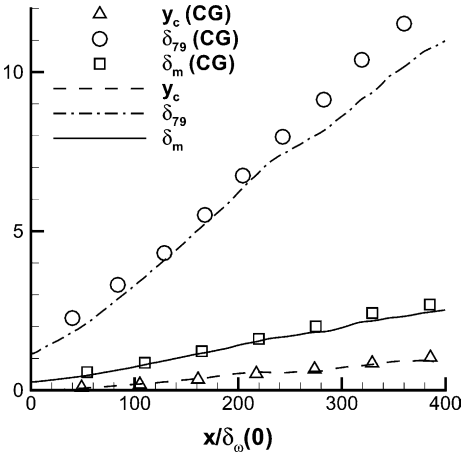

Fig. 6. Evolution of mixing layer. δ_m and δ_ω are the momentum thickness and the vorticity thickness [18], respectively. y_c is the transverse location of the mixing layer centerline. The symbol 'CG' represents the results from a coarse grid system.

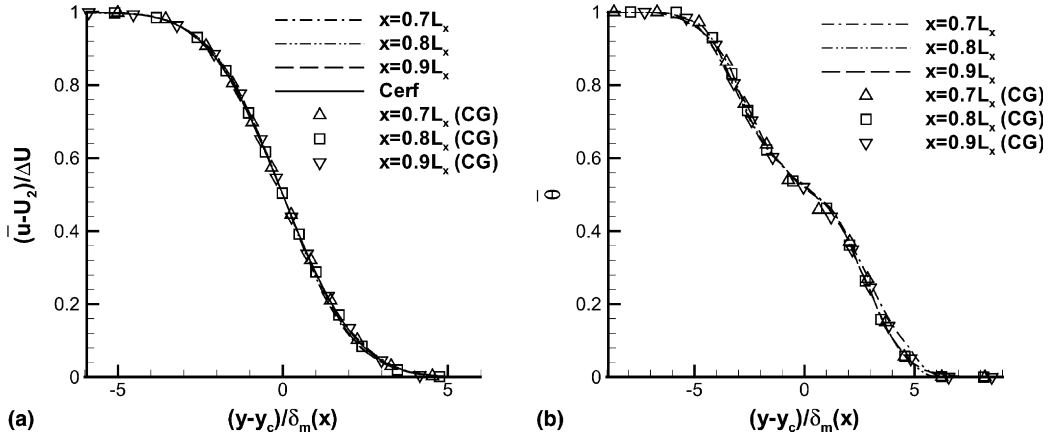

Fig. 7. Velocity (a) and scalar concentration (b) profiles at different streamwise locations.

comes from the pure fluid engulfed by the large structures [25,26]. The similarity also prevails in the scalar concentration fluctuation intensity profiles shown in Fig. 8. They have double peaks which come from the lack of both 3D variations and small-scale features in the simulation. The present result is consistent with other numerical results [24], but with better similarity and symmetry around the mixing layer center. The peak values agree well with the annular mixing layer [26] and larger than the experiment results [22]. The under-resolution of the measurement may explain this difference.

3.4. A shock hitting a helium cylindrical bubble

If the scalar function is assigned as the specific heat ratio of different gas, such as $\Theta = 1/(\gamma - 1)$, a so-called γ-model has been obtained [27] for compressible multi-fluids. Jiang and Ni [28] extended this model to an earlier BGK scheme without implementation of nonequilibrium state. Here, similarly we use the γ-model as the scalar function in the current scheme and apply it in the simulation of the interaction of

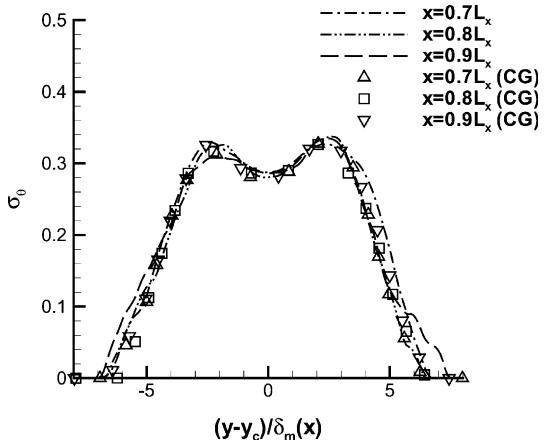

Fig. 8. Scalar fluctuation intensity profiles at different streamwise locations.

a $M_s = 1.22$ planar shockwave, moving in the air, and hitting with a cylindrical helium bubble [29–34]. As shown in Fig. 9 the initial flow distribution is determined from the standard shock relation with the given strength of the incident shock wave. The pre-shock gases are stationary. The conservative variables for the pre-shock air ($x < 225$) are $(\rho, p, \gamma) = (1.0, 1.0, 1.4)$ and $(0.1358, 1.0, 1.67)$ for the helium bubble, located at $x = 175$ with radius $r = 25$. The bubble is assumed to be in both thermal and mechanical equilibrium with the surrounding air. The computational cell size is $\Delta x = \Delta y = 0.25$ and reflecting boundary conditions are used on the upper and lower boundaries. The collision time is given by

$$\tau = 0.01\Delta t + \Delta t|p^r - p^l|/|p^r + p^l| \tag{34}$$

for the inviscid flow calculation.

The flow field at time $t = 125$ is also shown in Fig. 9 with the numerical Schlieren images. This picture is produced using the method described in [29] to accentuate weak flow features. The complex pattern of the material interface instability induced by the shock can be clearly seen. The complex reflected and a transmitted shock waves can also be observed. These phenomena are consistent with the previous experimental and numerical studies [31,34]. The unstable interfaces and turbulent mixing (see Fig. 10) are captured automatically by the present scheme, which is similar to the previous results from the multimaterial BGK scheme [29]. These unstable structures could be removed by many schemes with special treatments at the material interface.

In the above calculation, the viscosity coefficient is proportional to the time step, which is similar to any other flow solver for the inviscid Euler equations. In the following, we are going to test the problem but

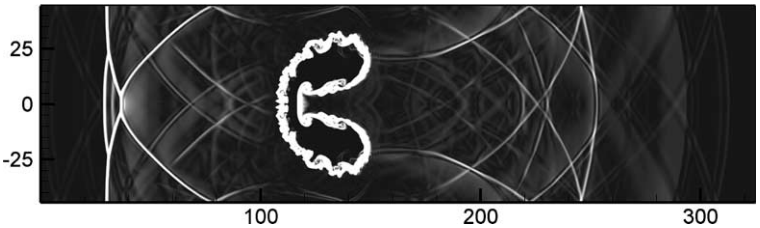

Fig. 9. Density fields of the interaction between $M_s = 1.22$ shock wave in the air and a helium cylindrical bubble. This numerical Schlieren image describes the density gradient distribution at time $t = 125$ (black = minimum, white = maximum).

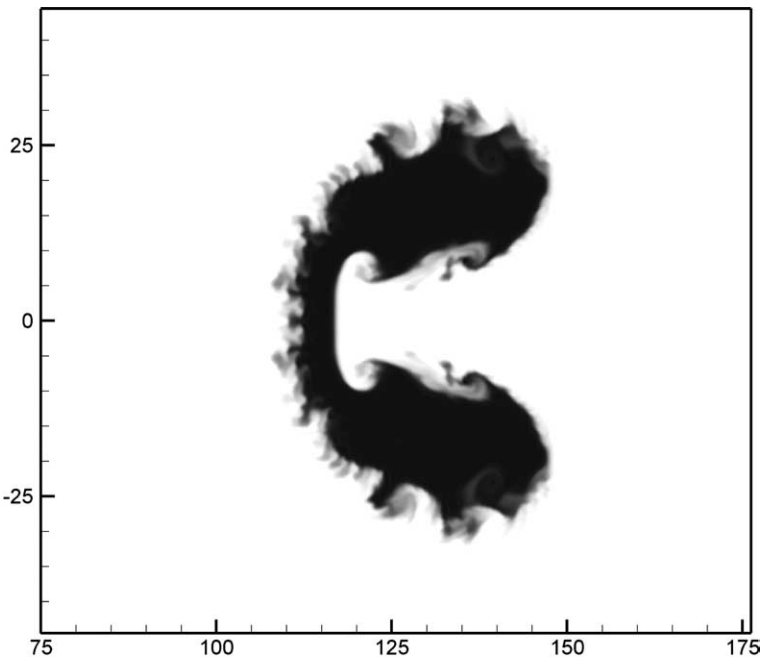

Fig. 10. The γ distribution of the shock bubble interaction at time $t = 125$. Black color represents the maximum value and white the minimum.

with fixed physical viscosity and heat conduction coefficients. If the collision time is calculated from the flow viscosity Eq. (20) with fixed kinematic viscosity coefficient $v = 0.05$, a grid-independent interface can be captured. This is shown in Fig. 11 in which the ρ and γ distributions along the central line computed on different cell size are nearly identical. This fact ensures the convergence of the current Navier–Stokes flow solver for the problems with diffusive interfaces, where the interface diffusion is governed by the advection–diffusion equation.

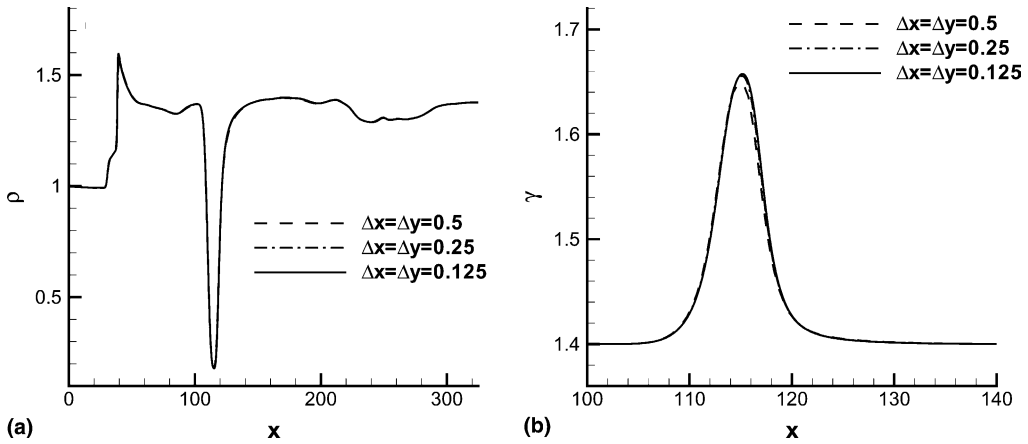

Fig. 11. The density (a) and specific heat ratio (b) profiles along the centerline for the shock-bubble interaction case at time $t = 125$.

3.5. A shock interaction with a SF6 cylinder

The present scheme is also examined with another type of shock bubble interaction. A shock in the air with $M_s = 1.2$ travels from left to right toward a cylindrical bubble (SF6) with an effective radius $R = 0.28$ cm [35]. The computational domain is 9.0 cm in the x direction and 1.5 cm in the y direction. Here due to the symmetry of the flow, only half of the flow field is calculated. Thus the symmetric condition is used at the lower y boundary ($y = 0$). At the top y boundary, reflection condition is enforced. At the inflow, the flow quantities are set according to the post-shock condition. The non-reflecting boundary condition is chosen at the right x boundary. The initial shock is located at $x = 0.25$ cm and the bubble center at $x = 0.8$ cm. The initial bubble density is given as a error function profile,

$$\rho = \frac{\rho_1 + \rho_2}{2} + \frac{\rho_1 - \rho_2}{2}\mathrm{erf}(r/\sigma), \tag{35}$$

where σ is a maximum slop thickness which is calculated from the interfacial transition layer thickness δ. In the present study, two cases are tested: $\sigma = \delta/3$ and $\sigma = \delta/5$. The subscript '1' denotes the air and '2' for the

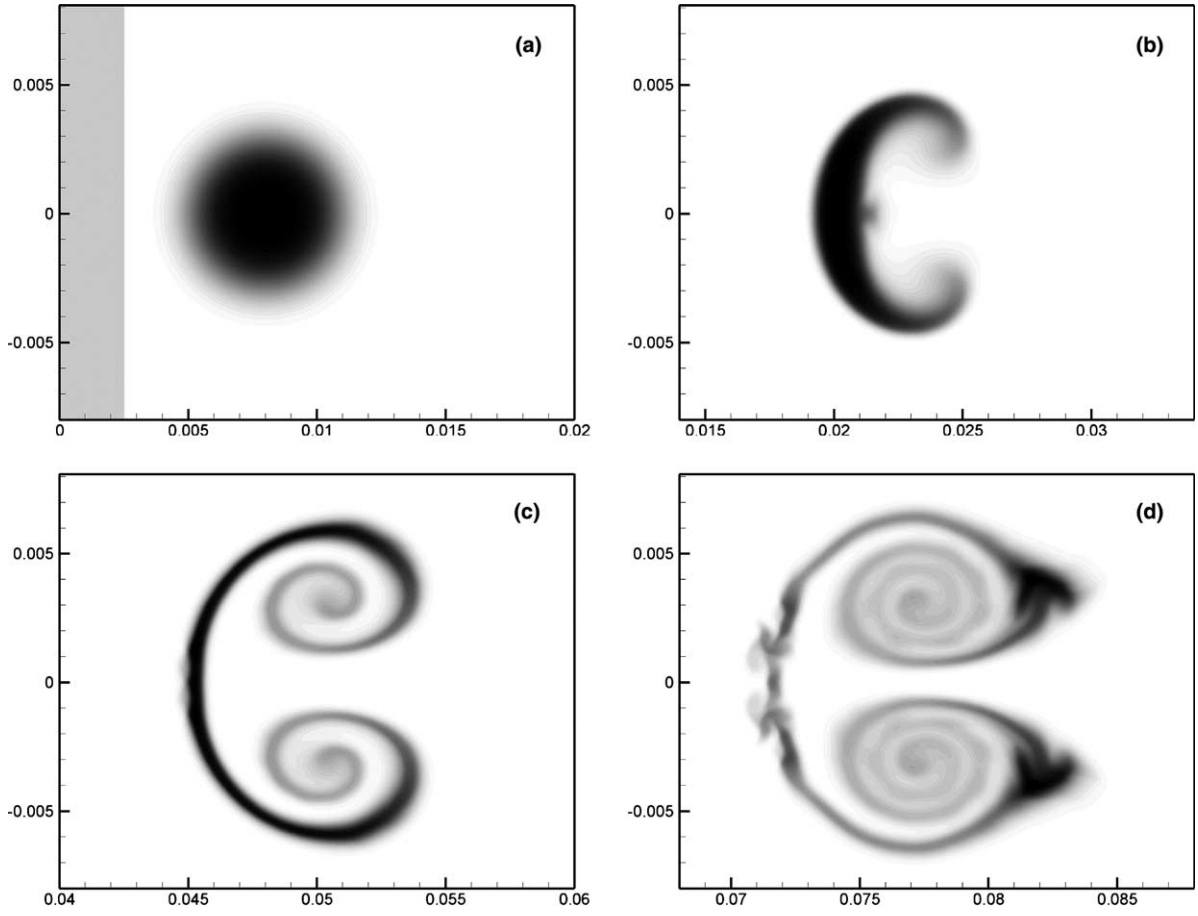

Fig. 12. A sequence of numerical images of the density fields in shock-SF6 cylinder interaction case. (a) The initial shock and bubble, (b) $t = 0.2$ ms, (c) $t = 0.5$ ms, and (d) $t = 0.8$ ms. The $M_s = 1.2$ shock wave passes from left to right and black represents the density with high value.

SF6 gas. Similar to the approach in [35], the specific heat ratios for both gases are fixed as $\gamma_1 = \gamma_2 = 1.4$. The density for SF6 is set as the 60% of the pure gas density $\rho_2 = 3.0$. The density for air is unity and the pressure for the stationary gases is 8.0×10^4 Pa. The collision time τ is computed as $\tau = 0.03\Delta t + \Delta t|p^r - p^l|/|p^r + p^l|$, with CFL number 0.4. 1500×250 uniform meshes are used in this case.

Fig. 12 shows the present calculated density fields at different times for the case $\sigma = \delta/5$. From these images the flow instability can be clearly seen: the heavy gas cylinder becomes flattening after the passage of the shock, forms a crescent shape, and then a vortex pair appears. The induced velocity wraps the SF6 gas to form a heavy gas strip. It is noticed that waves propagate from the upstream side of the heavy gas strip to the rear of the vortices. This computational flow pattern agrees well with the experimental observation [36]. The calculated bubble scales (shown in Fig. 13), normalized by the initial diameter of the bubble are also in fair agreement with experimental measurements [35]. In the present study, the bubble sizes are calculated through the density contour $\rho = 0.5(\rho_{1'} + \rho_{\max})$, where $\rho_{1'}$ is the post-shock air density and $\rho_{\max}$ is the local maximal. The present study shows that the initial density slope apparently affects the development of the bubble. The uncertainty in the experimental initial condition, the difference of the current 2D simulation from pseudo-2D experiments, along with coarse computational cell size, may contribute to the departure of the present results from the experimental values. The current method does not explicitly give any special numerical treatment in the interfaces. As shown in these figures, the interfaces calculated using the current scheme for the Richtmyer–Meshkov cases seem to be more actively unstable than other computations in the literatures. This definitely warrants the further investigation of the mechanism in the current numerical scheme, i.e., the effect of particle collision time on the interface instability. Much refined experimental measurements are also expected.

3.6. Rayleigh–Taylor instability

The Rayleigh–Taylor instability occurs at the interface between two fluids, when a light fluid is below a heavy one. Even though the current scheme is not targeted to this kind of flow, it can be still applied

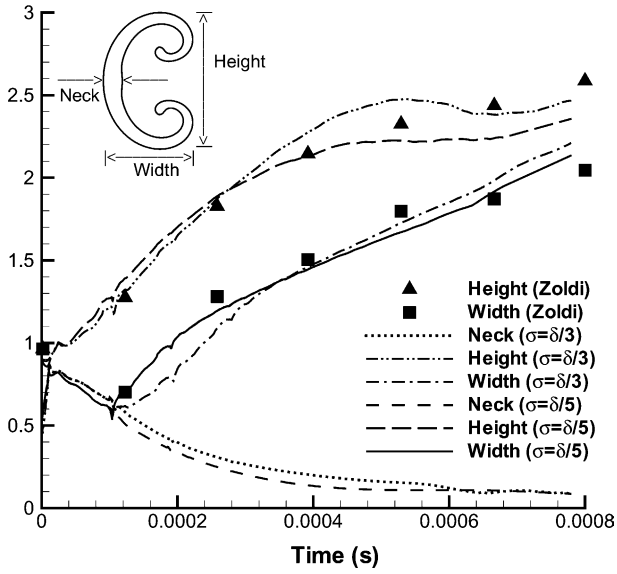

Fig. 13. Measurement of macroscopic scales. Width, height and neck, as defined in the figure and normalized by the initial diameter of the bubble. The symbol 'Zoldi' represents the experimental data from [35]. A shift of 0.02 ms is performed for the present curves to match the time scales between the simulation and experiment.

here, where an operator splitting procedure is used to treat the gravity source term. This computation is performed on a rectangular domain of $0 \leqslant x \leqslant 1$ and $-1 \leqslant y \leqslant 1$ with reflecting boundary conditions on the lower and upper sides of the domain and periodic ones in the horizontal direction. The gravity is along the $-y$ direction with non-dimensional gravitational constant $G = 0.5$. The densities close to the initial fluid interface at $y = y_s = 0.2$ are $\rho_1 = 0.5$ and $\rho_2 = 1.0$. Thus the Atwood number is $A = (\rho_2 - \rho_1)/(\rho_2 + \rho_1) = 1/3$. The pressure at the interface is $1/\gamma$, and the flow field are set with the isothermal conditions,

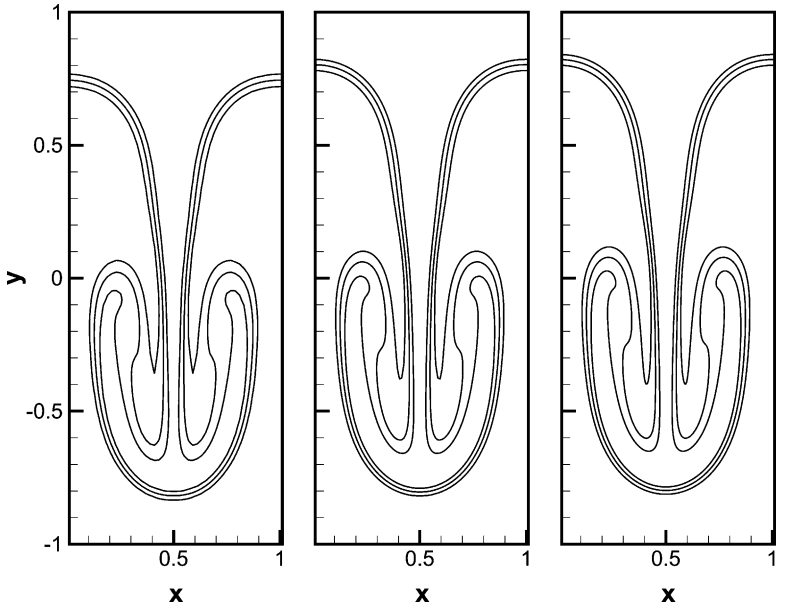

Fig. 14. Rayleigh–Taylor instability. The lines with the values of $\Theta = -0.5$, 0, 0.5 are plotted. From left to right, the mesh sizes used are $\Delta x = \Delta y = 0.02$, 0.01, 0.005 and the collision time keeps the same value $\tau = 4 \times 10^{-4}$ in all cases.

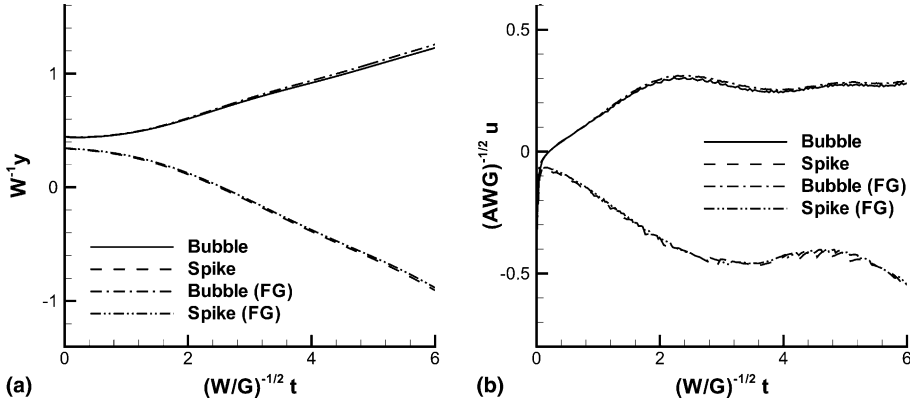

Fig. 15. Positions (a) and velocities (b) of the bubble and spike versus time for the Rayleigh–Taylor instability from a single mode perturbation. The symbol 'FG' represents the computation with a fine mesh.

$$\rho(y) = \begin{cases} \rho_1 \mathrm{e}^{-\gamma G(y-y_s)/T_1} & \text{if } y < y_s, \\ \rho_2 \mathrm{e}^{-\gamma G(y-y_s)/T_2} & \text{if } y > y_s, \end{cases} \tag{36}$$

where temperature $T_1 = \gamma p_s/\rho_1$ and $T_2 = \gamma\, p_s/\rho_2$. The initial scalar function has the values $\Theta = \pm 1.0$ below and above the interface, respectively. The initial velocity field is set to be zero. The density perturbation at the interface is added with the form $\delta\rho = 0.05[1 - \cos(2\pi x)]$ and the perturbation region is $y_s - 0.02 \leqslant y \leqslant y_s + 0.02$. In the current calculation the collision time is fixed to keep the same value of the physical viscosity.

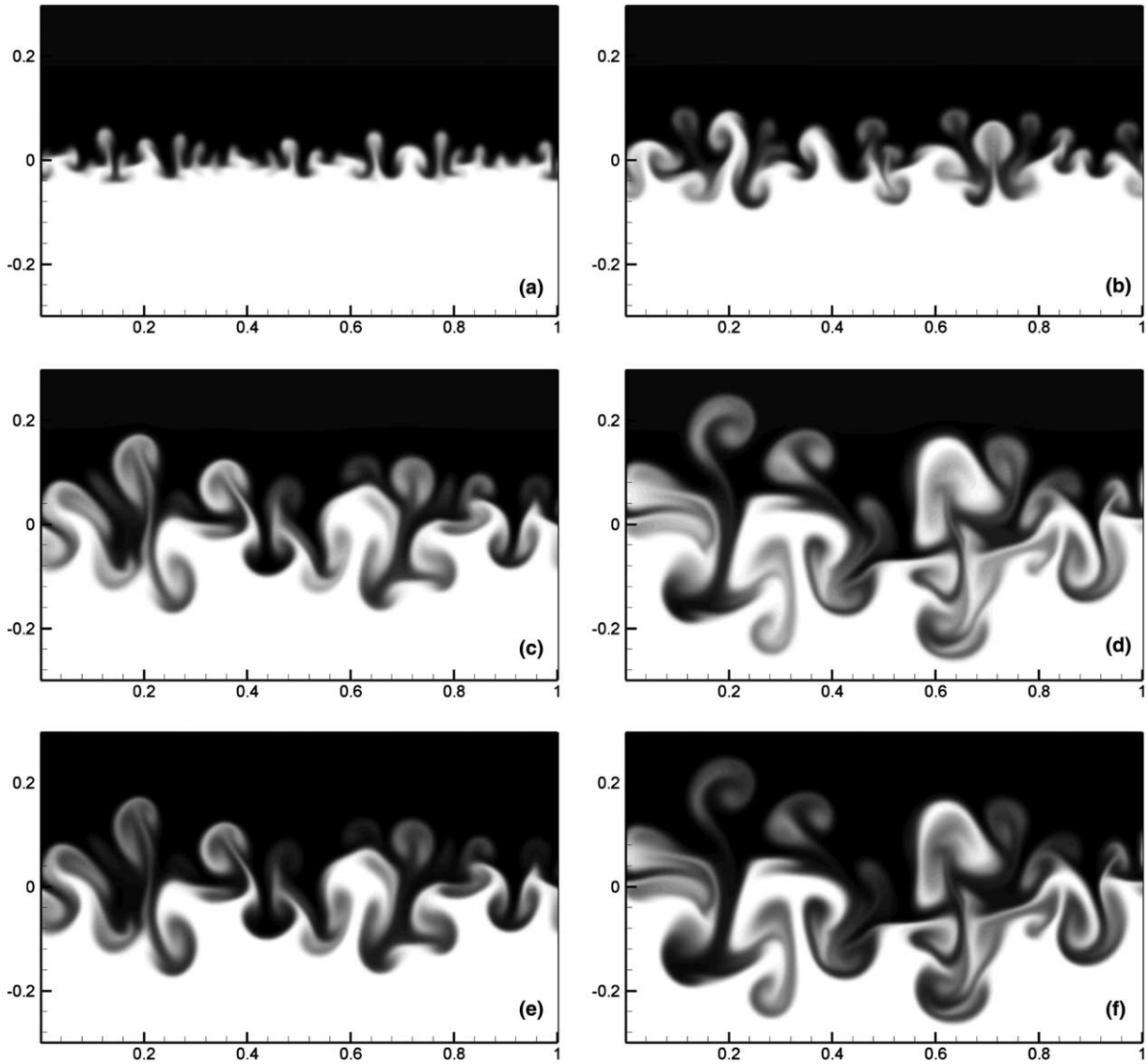

Fig. 16. Density (a–d) and scalar (e, f) fields of Rayleigh–Taylor instability from a multiple mode perturbation at different time measured in units of $\sqrt{W/G}$. (a) $t = 0.76$, (b) $t = 1.52$, (c, e) $t = 2.28$, and (d, f) $t = 3.04$.

Fig. 14 shows the computed scalar contours with values $\Theta = -0.5$, 0, 0.5 at time $t = 10.0$ on three different mesh sizes. It can be seen that with the mesh refinement, the results are basically identical. This shows again that the current NS solver could get converged numerical solution once the physical viscosity is fixed, and the interface is allowed to mix. If the Riemann solutions of the inviscid Euler equations are used in the flux evaluation, the numerical results usually do not converge with the mesh refinement [37,3].

To test the present scheme further, another case is calculated. The computational condition is same as the above, except that the initial perturbation is not for the density fields, but for the interface position with a single mode, $y_s = 0.2 + 0.05\cos(2\pi x)$. The computational domain is $W = 1.0$ (width) and $H = 4.0$ (height) with a uniform cell size $\Delta x = \Delta y = 0.01$. The dynamic viscosity is set to $v = 2.8 \times 10^{-4}$ and the gravitational constant $G = 0.1$. Fig. 15(a) shows the positions of the bubble front and spike tip versus time, obtained from the locations with scalar function $\Theta = 0$. After an early stage ($t/\sqrt{W/G} < 2$), the bubble front settles into a linearly developing state. The terminal bubble velocity, measured in units of $\sqrt{AgW}$ and shown in Fig. 15(b), is about 0.27. The growth of the spike shows a more complicated pattern. After an early-stage acceleration, when $t/\sqrt{W/G} > 3$, the spike slows down a little bit, then accelerates again. These phenomena agree well with the results of [38,39]. The computation with a fine mesh ($\Delta x = \Delta y = 0.005$) also validates the present result.

The Rayleigh–Taylor instability from a multiple mode perturbation is also studied with the present scheme. The computational domain is $W = 1.0$, $H = 1.2$ with uniform cell size in horizontal direction and stretched in the vertical direction. The ratio of the maximal and minimal cell size is about three. The mesh number is 640×800. The initial interface is given with multiple mode perturbation,

$$y_s = 0.0025 \sum_{n=11}^{30} \cos(2n\pi x/W + \varphi_n), \tag{37}$$

where the random phases, φ_n, are chosen from a uniform random distribution on the interval $0 \leqslant \varphi_n < 2\pi$. Fig. 16 shows the evolution of the flow at different time steps. The heavy fluid falls down as spikes while the light fluid rises up as small bubbles. Then the small structures interacts with each other and merge into larger ones, leading to a turbulent mixing layer. It is observed that the structure of the density field shows nearly identical to the scalar field, where the front of the bubble and the tip of the spike are defined as the positions with the horizontally averaged scalar value $\overline{\Theta} = \pm 0.98$, respectively. The result is shown in Fig. 17(a). Previous studies [40–43] have shown that the bubble front grows as αAgt^2 after an initial stage.

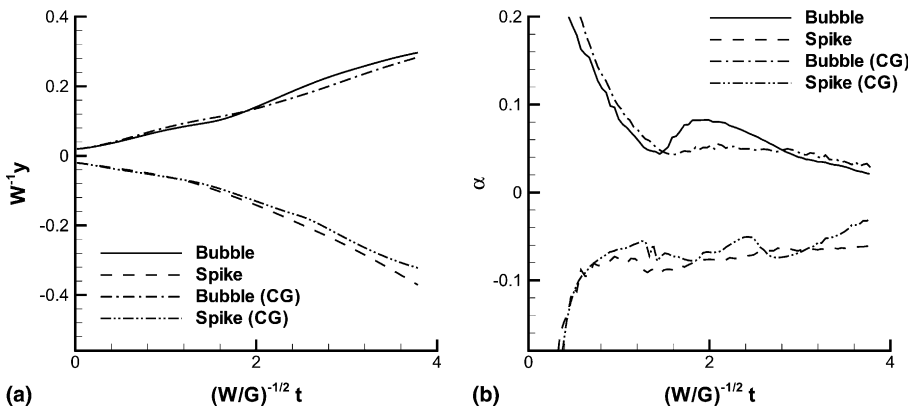

Fig. 17. Positions (a) and growth rate coefficients (b) of the bubble and spike versus time for the Rayleigh–Taylor instability from a multiple mode perturbation. The symbol 'CG' represents the computation with a coarse mesh with 400×500 cells.

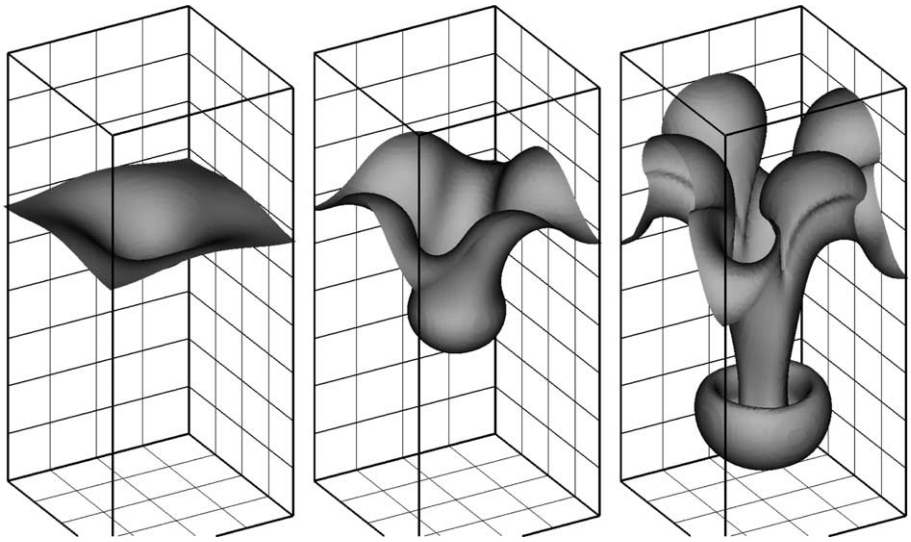

Fig. 18. Rayleigh–Taylor instability (3D case). From left to right, the iso-surfaces of $\Theta = 0$ are plotted at times $t = 4.0$, 6.0, 8.0, respectively. The mesh size is $\Delta x = \Delta y = \Delta z = 0.02$ and the collision time is $\tau = 4 \times 10^{-4}$.

In the present study, the coefficient α is calculated by $\alpha = \partial y_B/\partial(Agt^2)$, where y_B is the position of the bubble front. Fig. 17(b) shows the computed coefficient versus time. The value of α ranges between 0.04 and 0.08 in a mid stage, which agree with other studies [40,42,43].

The present scheme can be easily extended to 3D calculation. The scheme in 3D can be found in [44] for details. Fig. 18 shows the 3D computation of the Rayleigh–Taylor instability problem. The domain in the spanwise direction is $0 \leqslant z \leqslant 1$ and the periodic boundary conditions are used in this direction, as well as the horizontal direction. The initial density perturbation at the interface is given as $\delta\rho = 0.05[1 - \cos(2\pi x)][1 - \cos(2\pi z)]$. Other computational conditions are the same as the 2D case. It can be seen that the 3D instability is well captured by the present scheme.

4. Conclusion

The present paper introduces a new BGK-NS scheme with the inclusion of scalar function transport. In this scheme, an initial non-equilibrium state and a simplification on the evaluation of the temporal evolution part of the gas distribution function are implemented. This paper shows an easy and efficient way to extend from the existing gas-kinetic schemes to the equations with additional passive scalar transport. Since the flux for the scalar function is coupled with the other flow quantities, the present scheme not only keeps the accuracy of the BGK scheme for the Navier–Stokes equations, but also strengthens the scheme to be able to simulate the convective-diffusion scalar equation with a variable Schmidt number. Even though the objective of the current research is to accurately capture the Navier–Stokes diffusive interface and flow mixing, the scheme can also be used as a good interface capturing method when the non-mixing fluid interface is assigned with a certain value of the scalar function, such as the level set method. Many examples with complicated flow structure and interfaces are tested in this paper. The simulation results in the cases, such as the square wave convection and diffusion, the Rayleigh–Taylor instability, the supersonic mixing layer, confirm the validity of the current approach. The construction of the scheme with automatic anti-diffusive term in the under-resolved interface cases, is under investigation.

Acknowledgements

The authors thank reviewers for their helpful comments and suggestions. This work is supported by the National Natural Science Foundation of China (10302015, 10232020) and China Postdoctoral Science Foundation. K. Xu is supported by the Hong Kong Research Grant Council (HKUST6116/03E and 6102/04E).

Appendix A. Solution of matrix equation $\boldsymbol{b} = \boldsymbol{M}\boldsymbol{a}$

In the gas-kinetic scheme, the equation

$$\boldsymbol{b} = \boldsymbol{M}\boldsymbol{a} \tag{A.1}$$

is solved many times, where $\boldsymbol{b}$ and $\boldsymbol{M}$ are known. The matrix $\boldsymbol{M}$ is defined as $M_{\alpha_\beta} = (1/\rho)\int\psi_\alpha\,\psi_\beta\,g\mathrm{d}\Xi$. In 2D flow, $K = 3$, $\boldsymbol{b} = (b_1, b_2, b_3, b_4, b_5)^{\mathrm{T}}$, $\boldsymbol{a} = (a_1, a_2, a_3, a_4, a_5)^{\mathrm{T}}$, and

$$\boldsymbol{M} = \begin{pmatrix} 1 & U & V & C_1 & \Theta \\ U & U^2 + C_0 & UV & C_2 & U\Theta \\ V & UV & V^2 + C_0 & C_3 & V\Theta \\ C_1 & C_2 & C_3 & C_4 & C_1\Theta \\ \Theta & U\Theta & V\Theta & C_1\Theta & \Theta^2 + C_0 \end{pmatrix},$$

where

$$\begin{aligned} C_0 &= 1/(2\lambda), \\ C_1 &= \frac{1}{2}(U^2 + V^2 + (K+2)/(2\lambda)), \\ C_2 &= U(C_1 + 1/(2\lambda)), \\ C_3 &= V(C_1 + 1/(2\lambda)), \\ C_4 &= C_1^2 + C_1/\lambda - (K+2)/(8\lambda^2). \end{aligned}$$

Define

$$\begin{aligned} R_5 &= b_5 - \Theta b_1, \\ R_4 &= b_4 - C_1 b_1, \\ R_3 &= b_3 - V b_1, \\ R_2 &= b_2 - U b_1 \end{aligned}$$

the solution of (A.1) becomes

$$\begin{aligned} a_5 &= 2\lambda R_5, \\ a_4 &= \frac{8\lambda^2}{K+2}(R_4 - UR_2 - VR_3), \\ a_3 &= 2\lambda R_3 - V a_4, \\ a_2 &= 2\lambda R_2 - U a_4, \\ a_1 &= b_1 - U a_2 - V a_3 - C_1 a_4 - \Theta a_5. \end{aligned}$$

In 3D case, $\boldsymbol{b} = (b_1, b_2, b_3, b_4, b_5, b_6)^{\mathrm{T}}$, $\boldsymbol{a} = (a_1, a_2, a_3, a_4, a_5, a_6)^{\mathrm{T}}$, $K = 2$, and

$$\boldsymbol{M} = \begin{pmatrix} 1 & U & V & W & C_1 & \Theta \\ U & U^2 + C_0 & UV & UW & C_2 & U\Theta \\ V & UV & V^2 + C_0 & VW & C_3 & V\Theta \\ W & UW & VW & W^2 + C_0 & C_4 & W\Theta \\ C_1 & C_2 & C_3 & C_4 & C_5 & C_1\Theta \\ \Theta & U\Theta & V\Theta & W\Theta & C_1\Theta & \Theta^2 + C_0 \end{pmatrix},$$

where

$$C_0 = 1/(2\lambda)$$
$$C_1 = \frac{1}{2}(U^2 + V^2 + W^2 + (K+3)/(2\lambda))$$
$$C_2 = U(C_1 + 1/(2\lambda))$$
$$C_3 = V(C_1 + 1/(2\lambda))$$
$$C_4 = W(C_1 + 1/(2\lambda))$$
$$C_5 = C_1^2 - (K+1)C_1/(2\lambda) + (K+1)(K+3)/(16\lambda^2).$$

Similarly, define

$$R_6 = b_6 - \Theta b_1,$$
$$R_5 = b_5 - C_1 b_1,$$
$$R_4 = b_4 - W b_1,$$
$$R_3 = b_3 - V b_1,$$
$$R_2 = b_2 - U b_1,$$

the solution of (A.1) is

$$a_6 = 2\lambda R_6,$$
$$a_5 = \frac{8\lambda^2}{K+3}(R_5 - UR_2 - VR_3 - WR_4),$$
$$a_4 = 2\lambda R_4 - W a_5,$$
$$a_3 = 2\lambda R_3 - V a_5,$$
$$a_2 = 2\lambda R_2 - U a_5,$$
$$a_1 = b_1 - U a_2 - V a_3 - W a_4 - C_1 a_5 - \Theta a_6.$$

Appendix B. Diffusion coefficient from BGK equation

Let us consider the pure diffusion case which comes from the inhomogeneous abundance. The particles are all the same in the flow-field, but some of them are labeled with '1' and others '2'. The mass fraction for particle '1' is defined as Θ. The temperature T and the pressure p are uniform and the mass fraction variation is only in the x direction. The macroscopic velocity U is set to be zero. Thus, the diffusion flux for particle '1' is

$$J_1 = \rho_1 U_1 = \int u_1 f_1 \, \mathrm{d}u_1 \, \mathrm{d}\Xi, \tag{B.1}$$

where the distribution function of particle '1' satisfies the 1D BGK equation

$$\frac{\partial f_1}{\partial t} + u_1 \frac{\partial f_1}{\partial x} = \frac{g_1 - f_1}{\tau}. \tag{B.2}$$

Based on the equilibrium state

$$g_1 = \rho_1 (\lambda/\pi)^{(K+1)/2} \mathrm{e}^{-\lambda((u-U)^2+\xi^2)}, \tag{B.3}$$

where the internal degree of freedom $K = (3-\gamma)/(\gamma-1)$, the first-order approximation of the distribution function f_1 can be written as

$$f_1 = g_1 - \tau \frac{\partial g_1}{\partial t} - \tau u_1 \frac{\partial g_1}{\partial x}. \tag{B.4}$$

Substitute the above equation into (B.1), with $U = 0$ and $\rho_1 = \rho\Theta$, we have

$$\begin{aligned} J_1 &= \int u_1 g_1 \,\mathrm{d}u_1 \,\mathrm{d}\Xi - \int \tau u_1 \frac{\partial g_1}{\partial t} \,\mathrm{d}u_1 \,\mathrm{d}\Xi - \int \tau u_1^2 \frac{\partial g_1}{\partial x} \,\mathrm{d}u_1 \,\mathrm{d}\Xi \\ &= \rho_1 U - \tau \frac{\partial(\rho_1 U)}{\partial t} - \tau \frac{\partial}{\partial x}(\rho_1 U^2 + \rho_1/(2\lambda)) = -\tau \frac{\partial}{\partial x}(\rho\Theta/(2\lambda)) = -\tau p \frac{\partial \Theta}{\partial x}. \end{aligned} \tag{B.5}$$

Comparing the above relation with Fick's Law, the diffusion coefficient can be easily obtained,

$$D = \tau p/\rho = v. \tag{B.6}$$

References

[1] K. Xu, A gas-kinetic BGK scheme for the Navier–Stokes equations, and its connection with artificial dissipation and Godunov method, J. Comput. Phys. 171 (2001) 289–335.
[2] K. Xu, M. Mao, L. Tang, A multidimensional gas-kinetic BGK scheme for hypersonic viscous flow, J. Comput. Phys. (to appear).
[3] Y.S. Lian, K. Xu, A gas-kinetic sheme for reactive flows, Comput. Fluids 29 (2000) 725–748.
[4] Q.B. Li, S. Fu, A new simplified gas-kinetic BGK scheme, Chin. J. Comput. Phys. 19 (6) (2002) 471–475.
[5] S. Osher, J.A. Sethian, Fronts propagating with curvature dependent speed: algorithms based on Hamilton–Jacobi formulations, J. Comput. Phys. 79 (1988) 12–49.
[6] J.A. Sethian, P. Smereka, Level set methods for fluid interfaces, Annu. Rev. Fluid Mech. 35 (2003) 341–372.
[7] K. Xu, A. Jameson, Gas-kinetic relaxation (BGK-type) schemes for the compressible Euler equations, AIAA Paper 95-1736 (1995).
[8] Y.S. Lian, R.Q. Wang, Simplified BGK-type scheme, Chin. J. Comput. Mech. 16 (3) (1999) 275–281.
[9] T. Ohwada, On the construction of kinetic schemes, J. Comput. Phys. 177 (1) (2002) 156–175.
[10] J. Zhao, Q.B. Li, G. Zhang, S. Fu, Numerical simulation of gas flow in micro-channels with bgk scheme, J. Tsinghua Univ. (Sci. & Tech.) 43 (8) (2003) 1083–1087.
[11] P.R. Woodward, P. Colella, The numerical simulation of two-dimensional fluid flow with strong shocks, J. Comput. Phys. 54 (1984) 115–173.
[12] G.L. Brown, A. Roshko, On density effects and large structures in turbulent mixing layers, J. Fluid Mech. 64 (4) (1974) 775–816.
[13] D. Papamoschou, A. Roshko, The compressible turbulent shear layer: an experimental study, J. Fluid Mech. 197 (1988) 453–477.
[14] T. Rossmann, M.G. Mungal, R.K. Hanson, Evolution and growth of large-scale structures in high compressibility mixing layers, J. Turbulence 3 (2002) 009.
[15] S.K. Lele, Direct numerical simulation of compressible free shear flows, AIAA Paper 89-0374 (1989).
[16] C. Pantano, S. Sarkar, A study of compressibility effects in the high-speed turbulent shear layer using direct simulation, J. Fluid Mech. 451 (2002) 329–371.
[17] Q.B. Li, S. Fu, Budget of transportatoin of compressible mixing layer, J. Tsinghua Univ. (Sci. & Tech.) 42 (8) (2002) 1087–1090.
[18] Q.B. Li, S. Fu, Numerical simulation of high-speed planar mixing layer, Comput. Fluids 32 (2003) 1357–1377.
[19] Q.B. Li, H.X. Chen, S. Fu, Large-scale vortices in high-speed mixing layers, Phys. Fluids 15 (2003) 3240–3244.
[20] S.G. Goebel, J.C. Dutton, Experimental study of compressible turbulent mixing layers, AIAA J. 29 (1991) 538–546.

[21] M.M. Koochesfahani, P.E. Dimotakis, Laser-induced fluorescence measurements of mixed fluid concentration in a liquid plane mixing layer, AIAA J. 23 (11) (1985) 1700–1707.
[22] N.T. Clemens, M.G. Mungal, Large-scale structure and entrainment in the supersonic mixing layer, J. Fluid Mech. 284 (1995) 171–216.
[23] N.D. Sandham, W.C. Reynolds, Some inlet-plane effects on the numerically simulated sptially-developing mixing layer, in: J.C. Andre, J. Cousteix, F. Durst, B.E. Launder, F.W. Schmidt, J.H. Whitelaw (Eds.), Turbulent Shear Flows 6, Springer, Berlin, 1989, pp. 441–454.
[24] C.K. Oh, E. Loth, Unstructured grid simulations of spatially evolving supersonic shear layers, AIAA J. 33 (7) (1995) 1229–1238.
[25] M.M. Rogers, R.D. Moser, Direct simulation of a self-similar turbulent mixing layer, Phys. Fluids 6 (2) (1994) 903–923.
[26] J.B. Freund, S.K. Lele, P. Moin, Compressibility effects in an turbulent annular mixing layer: Part 1. turbulence and growth rate, J. Fluid Mech. 421 (2000) 229–267.
[27] R. Abgrall, How to prevent pressure oscillations in multicomponent flow calculation: a quasi conservative approach, J. Comput. Phys. 125 (1996) 150–160.
[28] S. Jiang, G. Ni, A γ-model BGK scheme for compressible multifluids, Int. J. Numer. Methods Fluids 46 (2) (2004) 163–182.
[29] Y.S. Lian, K. Xu, A gas-kinetic sheme for multimaterial folws and its application in chemical reaction, J. Comput. Phys. 163 (2000) 349–375.
[30] J.F. Haas, B. Sturtevant, Interactions of weak shock waves with cylindrical and spherical gas inhomogeneities, J. Fluid Mech. 181 (1987) 41–76.
[31] J.J. Quirk, S. Karni, On the dynamics of a shock bubble interaction, J. Fluid Mech. 318 (1996) 129–163.
[32] R.P. Fedkiw, X.D. Liu, S. Osher, A non-oscillatory eulerian approach to interfaces in multimaterial flows (the ghost fluid method), J. Comput. Phys. 152 (1999) 457–492.
[33] M. Brouillette, The Richtmyer–Meshkov instability, Annu. Rev. Fluid Mech. 34 (2002) 445–468.
[34] C. Matsuoka, K. Nishihara, Y. Fukuda, Nonlinear evolution of an interface in the Richtmyer–Meshkov instability, Phys. Rev. E 67 (2003) 036301.
[35] S. Zhang, N.J. Zabusky, G. Peng, S. Gupta, Shock gaseous cylinder interactions: dynamically validated initial conditions provide excellent agreement between experiments and numerical simulation to late-intermediate time, Phys. Fluids 16 (5) (2004) 1203–1216.
[36] J.W. Jacobs, The dynamics of shock accelerated light and heavy gas cylinders, Phys. Fluids A 5 (1993) 2239–2247.
[37] M. Mulder, S. Osher, J.A. Sethian, Computing interface motion in compressible gas dynamics, J. Comput. Phys. 100 (1992) 209–228.
[38] G. Tryggvason, Numerical simulation of the Rayleigh–Taylor instability, J. Comput. Phys. 75 (1988) 253.
[39] X. He, S. Chen, R. Zhang, A lattice Boltzmann scheme for incompressible multiphase flow and its application in simulation of Rayleigh–Taylor instability, J. Comput. Phys. 152 (1999) 642–663.
[40] D.L. Youngs, Numerical simulation of turbulent mixing by Rayleigh–Taylor instability, Physica D 12 (1984) 32.
[41] K.I. Read, Experimental investigation on turbulent mixing by Rayleigh–Taylor instability, Physica D 12 (1984) 45.
[42] E. George, J. Glimm, X.L. Li, A. Marchese, Z.L. Xu, A comparison of experimental, theoretical, and numerical simulation Rayleigh–Taylor mixing rates, Proc. Natl. Acad. Sci. USA 99 (2002) 2587–2592.
[43] T.T. Clark, A numerical study of the statistics of a two-dimensional Rayleigh–Taylor mixing layer, Phys. Fluids 15 (8) (2003) 2413–2423.
[44] Q.B. Li, Numerical study of compressible mixing layer with BGK scheme, Ph.D. thesis, Tsinghua University, Beijing (2002).